

CONFERENCES AND SYMPOSIA

PACS numbers: 95.55.Ka, **96.60.–j**, 96.60.qe

X-ray and gamma-ray emission from solar flares

A L Lysenko, D D Frederiks, G D Fleishman, R L Aptekar, A T Altyntsev, S V Golenetskii, D S Svinkin, M V Ulanov, A E Tsvetkova, A V Ridnaia

DOI: https://doi.org/10.3367/UFNe.2019.06.038757

Contents

Abstract. **We present a brief review of the contemporary understanding of and topical problems in solar flare physics that can be clarified by methods of X-ray and gamma-ray astronomy. The review focuses on several issues, including the conditions and mechanisms of electron acceleration in solar flares, the flare energy distribution between thermal and nonthermal components, the gamma-ray emission from solar flares and its dynamics, and the spatial structure of X-ray and gamma-ray sources. Discussed in this context are the latest data obtained by the joint Russia–US experiment Konus-Wind, which in 2019 celebrated the 25th anniversary of continuous operation in space.**

Keywords: heliophysics, solar flares, X-ray and gamma-ray astronomy

A L Lysenko [1, a], **D D Frederiks** [1, b], **G D Fleishman** [1, 2, c], **R L Aptekar** [1, d], **A T Altyntsev** [3, e], **S V Golenetskii** [1, f], **D S Svinkin** [1, g], **M V Ulanov** [1, h], **A E Tsvetkova** [1, i], **A V Ridnaia** [1, j]

[1] Ioffe Institute, Politekhnicheskaya 26, 194021 St. Petersburg, Russian Federation

[2] New Jersey Institute of Technology, University Heights, Newark, NJ 07102-1982, USA

[3] Institute of Solar-Terrestrial Physics, ul. Lermontova 126A, 664033 Irkutsk, Russian Federation

E-mail: [a] alexandra.lysenko@mail.ioffe.ru, [b] fred@mail.ioffe.ru, [c] gregory@sun.ioffe.rssi.ru, [c] gfleishm@njit.edu, [d] aptekar@mail.ioffe.ru, [e] altyntsev@iszf.irk.ru, [f] golen@mail.ioffe.ru, [g] svinkin@mail.ioffe.ru, [h] ulanov@mail.ioffe.ru, [i] tsvetkova@mail.ioffe.ru, [j] ridnaia@mail.ioffe.ru

Received 5 June 2019

Uspekhi Fizicheskikh Nauk **190** (8) 878 – 894 (2020)

Translated by E N Ragozin; edited by A M Semikhatov

1. Introduction

Life on Earth is directly dependent on our closest star, the Sun, which provides most of our heat and light. Humanity has recognized this for many millennia of its history. However, with the development of modern technologies, including space-based ones, it turned out that the role played by the Sun is highly diversified, and that certain manifestations of solar activity can be hazardous to the technological infrastructure and human health.

The manifestations of solar activity are quite numerous: evolving coronal magnetic loops and jets observed in the ultraviolet part of the spectrum from satellites; coronal mass ejections recorded in a broad wavelength range, from the radio range to the ultraviolet one; solar flares — relatively short-term strong local brightenings observed throughout the electromagnetic spectrum, from radio waves to hard gamma rays; and many others. Quite frequently, these phenomena are beautiful and majestic, but to an even greater extent they are complicated for quantitative understanding.

Solar activity is caused by solar magnetism — a system of dynamic effects controlling the generation of the magnetic field and attendant electric currents, their evolution, dissipation, and conversion to the energy of heat, particle acceleration, and large-scale plasma motion. Following the motions of subphotospheric plasma, the evolution of an active region results in the enhancement of electric currents and accumulation of free magnetic energy. One part of this energy almost continuously dissipates into thermal energy, while the other part can lead to an explosive energy release due to one instability or another. During a solar flare, the magnetic energy stored in a relatively large volume of the magnetized corona is catastrophically released in a short time, of the order of several minutes or even seconds, as a result of a complex of phenomena generically called 'magnetic reconnection' [1, 2]. The flares are frequently attended by a large-scale restructuring of the magnetic field as well as by a variety of secondary manifestations (for instance, polar lights observed even on other planets of the Solar System [3]).

Magnetic reconnection events, which are accompanied by plasma heating and charged particle acceleration, are responsible for many transient phenomena observed in the Universe on the extremely broad scales of distance, luminosity, and energy release. Specifically, manifestations of magnetic reconnection have been recorded in highly different parts of the Solar System: on the Sun [4, 5], in the terrestrial magnetosphere [6, 7], in cometary tails [8], and in the solar wind [9, 10]. It is likely that magnetic reconnection plays an important role in many astrophysical phenomena and objects like cosmological gamma-ray bursts [11–13], the origin of large-scale radio structures ('arcs' and 'fibers') in the galactic center region [14], microquasars [15], the X-ray emission of the hot component of the interstellar medium [16], particle acceleration in the accretion disks of the active galactic nuclei [17, 18], and flares on highly magnetized neutron stars, so-called magnetars [19–21].

Solar research permits obtaining limitations on the parameters of stellar models, in particular, the stellar magnetic field and stellar activity cycles [22–24], the stellar wind [25–26], mass ejections [27], and the dynamics of stellar flare emission [28]. Consequently, it is hard to overestimate the importance of solar studies, where the structure of the magnetic field, the acceleration of particles, and their propagation and interactions can be studied on different spatio-temporal scales, including relatively short ones. This detailed observational information is required for understanding dynamic processes resulting in magnetic reconnection and its attendant phenomena, for the physics of solar–terrestrial connections, for space weather forecasting, and for addressing crucial astrobiology questions.

2. Contemporary view of solar flares

2.1 Observations of solar flares

Solar activity is characterized by periodicity on different time scales (from 158 days to several millennia) [29, 30], among which the 11-year activity cycle is most pronounced. To indicate solar activity, the relative number of sunspots (the Wolf number) is often used, which typically correlates well with the number of solar flares.

The first described observation of a solar flare was made near the peak of solar activity, on September 1, 1859, when the British astronomer Robert Carrington observed a solar flare in the optical region [31]. That flare was accompanied by a major coronal mass ejection (CME) and the most powerful geomagnetic storm in history, which has come to be known as the 'Carrington event'.

Since then, the methods of astronomical observations, in particular of solar observations, have radically changed, and astronomy has turned from an optical science into an all-wavelength science. For instance, the discovery of solar activity in the radio range was closely related to the progress of radar during World War II and was first described in the scientific literature shortly after its end [32].

With the onset of the space era, observations in the infrared, ultraviolet, X-ray, and gamma-ray ranges of the electromagnetic spectrum became available, while technological progress made it possible to extend radio observations to the millimeter and submillimeter parts of the spectrum.

Observations of high-energy electromagnetic solar radiation became possible with the onset of extra-atmospheric astronomy in the middle of the 20th century. The first long-lasting experiment on the measurement of X-ray fluxes was performed aboard the Sputnik-2 spacecraft launched on November 3, 1957 [33], and in 1963–1965 it was possible to directly photograph the Sun in the X-ray and far ultraviolet spectral ranges with pinhole camera techniques aboard geophysical rockets [34, 35].

The first space telescope of the GOES (Geostationary Operational Environmental Satellite) series was launched in 1975. It was intended to continuously monitor soft X-ray solar emission. The operation of the spacecraft of this series continues, with GOES-15, GOES-16, and GOES-17 now in operation. The soft X-ray fluxes in two broad GOES channels (1–8 Å and 0.5–4 Å) provide the basis for the most common classification of solar flares in terms of their power (Classes A, B, C, M, and X).

The history of solar activity observations with spacecraft in the hard X-ray and gamma-ray ranges in the recent decades is schematically presented in Fig. 1.

A large contribution to the observations of high-energy solar emission was made by the Solar Maximum Mission (SMM) observatory [36], which operated from February 1980 through December 1989.

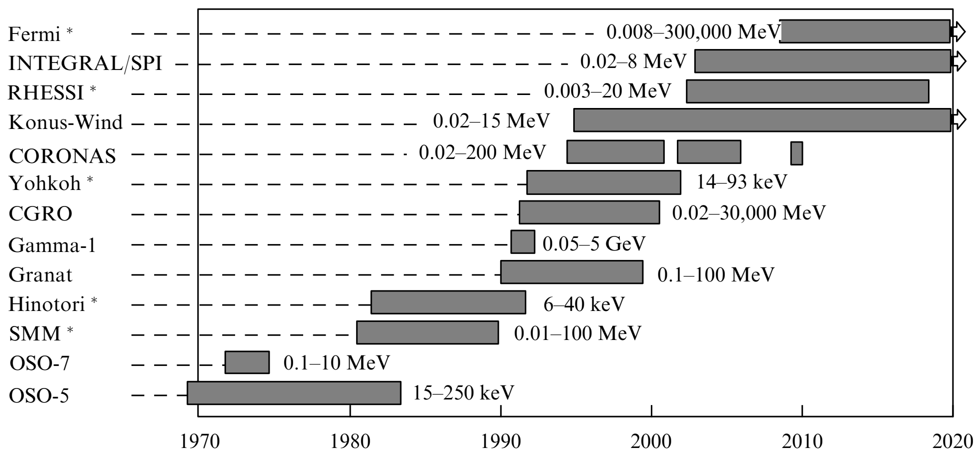

Figure 1. Hard X-ray and gamma-ray observations of solar activity aboard spacecraft over recent decades. Experiments with the capacity of imaging are indicated by asterisks. CGRO: Compton Gamma-Ray Observatory. OSO: Orbital Solar Observatory. Other abbreviations are defined in the text.

Important results were obtained by the telescopes that imaged the Sun in the hard X-ray range of the electromagnetic spectrum. The geometry of flare sources in the soft and hard X-ray ranges was investigated by the Soft X-ray Telescope (SXT) and Hard X-ray Telescope (HXT) of the Japan space Yohkoh observatory (1991–2001) and American RHESSI (Reuven Ramaty High Energy Solar Spectroscopic Imager) observatory (2002–2018) [37]. The outstanding success of the solar flare research by RHESSI [38–42] was due to the combination of high spatial and spectral resolutions, which permitted X-ray imaging in different energy intervals, thereby separating the contributions of different kinds of emission. Among the RHESSI limitations, we mention the relatively low temporal resolution, 4 s, which was caused by the spacecraft rotation period and was insufficient for diagnosing particle acceleration on the shortest time scale [43], as well as the long gaps in observations due to the spacecraft passage through the South Atlantic anomaly and its shading by Earth.

Among domestic tools, we select the Gamma-1 experiment, which performed observations in the energy range up to 5 GeV [44] in 1990–1992. From 1994 to 2009, the CORONAS series (Complex orbital near-Earth observations of solar activity) of solar space observatories operated intermittently, replacing each other. On one of them, CORANAS-F, an experiment entitled SONG (SOlar Neutrons and Gamma rays), was carried out in 2001–2005, involving the capacity to detect high-energy emission in the range 0.05–140 MeV. Apart from the gamma rays, the instrument registered neutrons with energies above 20 MeV [45]. Another instrument of the CORONAS-F observatory, the Helicon gamma-ray spectrometer, performed observations in the energy range 10 keV–10 MeV [46].

At present, solar observation data in the hard X-ray and gamma-ray ranges are provided by the Konus-Wind [47], Fermi-GBM (Gamma-ray Burst Monitor) [48], and Fermi-LAT (Large Area Telescope) [49] missions, as well as by the spacecraft Integral (International Gamma Ray Astrophysics Laboratory) [50], which were initially designed to primarily study objects outside the Solar System but also made a significant contribution to the development of solar physics [51–54].

2.2 Models of solar flares, their origin and energy characteristics

Solar flares are initiated above active regions in the solar corona dominated by the energy of the magnetic field [56]. In the active regions, the magnetic field is quite strong: the photospheric magnetic field can be as high as 6 kG [57–59] and the coronal one can range up to 4 kG [60] at the corona base and to several hundred Gauss at an altitude of 20–30 Mm [2, 61, 62]. The degree of 'magnetization' of the solar plasma is commonly characterized by the parameter termed the 'plasma beta' (β), equal to the gas-kinetic pressure to the magnetic pressure ratio. Typical β values in the corona are of the order of 0.001–0.01, which means that in the corona there are no forces that could equilibrate the magnetic component of the Lorentz force. Therefore, in a stationary state, the electric current should be directed almost along the magnetic field, which results in 'force-free' configurations of the magnetic field. Nonstationary processes occurring under variations in the local magnetic field configuration result in dynamic phenomena like solar flares, mass ejections, and jets.

Developed in the 1960s–1970s, the 'standard model' of a solar flare [63–66] implies the release of energy stored in the

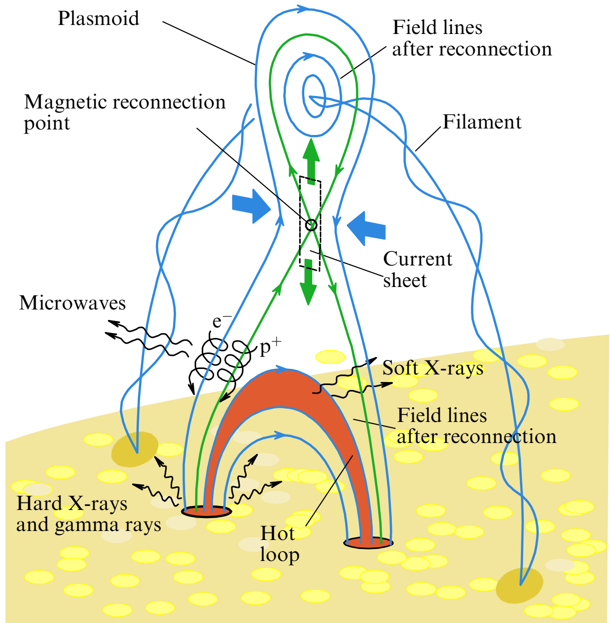

Figure 2. (Color online.) Standard model of a solar flare. The flare is triggered by the ascension of a filament, which results in magnetic reconnection, the inflow of cool plasma from the loop sides (blue arrows), and the outflow of hot plasma upwards and downwards (green arrows). The helices show the motion of electrons and ions, accelerated due to the reconnection, along the field lines towards the loop footpoints, where they give rise to hard X-rays (XRs) and gamma rays. As a result of deceleration of the charged particles, the plasma of the solar atmosphere heats up, evaporates, fills the post-flare loops, and emits in the soft X-ray range. (Drawing adapted from Ref. [55].)

nonpotential magnetic field of an active region due to its rapid restructuring, 'magnetic reconnection'. According to the model, the reconnection occurs in the current sheet near the neutral point of a flare loop (Fig. 2) located in the solar corona at an altitude of several tens of thousands of kilometers. The magnetic reconnection can be triggered by the ascension of a filament [63] (the magnetic tube in Fig. 2) or the twisting of the loop due to the displacement of its footpoints relative to each other [64]. In both cases, the standard model implies the ejection (eruption) of macroscopic volumes of coronal plasma — the ascending plasmoid in Fig. 2. The plasmoid is a plasma volume bounded by a twisted magnetic tube [55], which subsequently transforms into a CME.

The energy released due to reconnection is spent on the kinetic energy of the plasmoid, direct heating of the ambient plasma, and accelerating charged particles: electrons and ions.

Some of the accelerated particles escape from the Sun and can be subsequently registered in the interplanetary space as the solar cosmic rays (SCRs), whose energy amounts to several GeV per nucleon for ions [67, 68] and several MeV for electrons [69, 70]. The others, which are mostly responsible for the electromagnetic flare emission, are captured by magnetic traps or travel along the magnetic field lines downwards, to the solar surface.

The kinematics of this part of the accelerated particles can be conventionally divided into five conceptually different physical processes (although some of them may overlap in time and/or in space): the acceleration of the particles, their injection into the flare loop, propagation in the loop, capture in a trap, and precipitation to the loop footpoints. When traveling in the loop, the electrons produce the gyrosynchrotron emission observed at frequencies from below 1 GHz to several tens or hundreds of GHz. On reaching the dense solar chromosphere, nonthermal electrons undergo frequent collisions with the ambient plasma ions and generate high-intensity bremsstrahlung. This emission is observed in the hard X-ray and gamma-ray ranges at energies up to several tens and hundreds of keV and, in some flares, up to ~ 10 MeV (this problem is discussed at greater length in Section 4). Under the action of accelerated high-energy particles that precipitate in the chromospheric footpoints of coronal magnetic loops, the chromospheric plasma heats and expands, and the Maxwellian (thermalized) electrons produce the bremsstrahlung observed in the soft X-ray, ultraviolet, and radio ranges.

Owing to their greater mass, the ions in the solar atmosphere lose energy less efficiently than electrons, and therefore their bremsstrahlung intensity is by far lower. The accelerated ions are detected primarily from the gamma-ray emission due to nuclear reactions with the ambient plasma ions. The gamma-ray emission of solar flares is observed both in nuclear lines (energies $\sim 1-10$ MeV) and in the high-energy continuum (energies $\gtrsim 10$ MeV) [71, 72].

The electrons that move along a flare loop with relatively large pitch angles, i.e., at large angles relative to the local magnetic field vector, can be reflected from the domain with a strong magnetic field and captured by magnetic traps [73]. Moving in a magnetic trap, electrons lose energy to gyrosynchrotron emission in the microwave range and to collisions with the ambient plasma.

Quite often observed in solar flares is a high correlation between the temporal profile of soft X-ray emission and the time integral of the emission profiles in the hard X-ray and microwave ranges (the Neupert effect [74]). An interpretation of this effect is that in these events the initially free magnetic energy transforms into the energy of accelerated nonthermal particles, which then spend it to heat the ambient plasma. The plasma cooling proceeds more slowly than its heating by the accelerated particles. Therefore, the nonthermal energy is 'accumulated' in the plasma and is gradually emitted in the soft X-ray, ultraviolet, and optical ranges.

The standard model described above is well suited to explain the morphology of many, but far from all, observed phenomena that attend solar flares. Readers may familiarize themselves with a broad, although not exhaustive, list of alternative topological models (and those complementary to the standard model) on the site of the Space Sciences Laboratory, University of California, Berkeley: http://solarmuri.ssl.berkeley.edu/~hhudson/cartoons. Among them, we single out the models of flares occurring due to the interaction of two or more closely located magnetic loops [53, 75–78]. These models describe many 'compact' flares not attended by ejections [79].

The limitation of the standard model can be illustrated, for instance, by comparing the magnetic (quite modest) energy confined in the current sheet with the energy released in a flare. The difference between them amounts to several orders of magnitude [2], and hence the magnetic energy release should occur in a volume much greater than the volume of the current sheet. A similar inference is suggested by an analysis of the 'electron number problem': up to 10^{36} electrons can be accelerated in a flare. For typical coronal plasma densities, they must occupy a volume of 10–100 Mm^3 [80], which is much larger than the current sheet volume. In the framework of the standard model, a variety of contradictions also emerges at the level of microscopic physics of particle acceleration and propagation, such as the problem of high return currents, which inevitably arise from directed motion of charged particles in the plasma [81–83]. Based on microwave data with high spatial and spectral resolution, it was recently shown in [2] that the sharp decay of the magnetic field in a flare occurs in a volume that is much greater than the volume of the current sheet, namely, in the entire volume of the 'cusp': from the reconnection point to the hot loop (see Fig. 2).

Solar flares are the highest-energy events in the Solar System. In Ref. [84], for 38 eruptive flares estimates were made of the total budget of free magnetic energy and the energy of individual flare components, including the energy of the thermal radiation of the heated plasma, the accelerated electron and ion energies, and the CME energy. For the events under consideration, the free magnetic energy of the flares was in the range $(1\text{–}30) \times 10^{32}$ erg. On average for the sampling, CMEs account for the bulk ($\sim 20\%$) of energy dissipation, the energy of accelerated particles accounts for $\sim 6\%$, while the energy of thermal plasma emission in the soft X-ray range accounts for only about 1%. In this case, no correlation was observed between the amount of energy in one channel or another for an individual event.

2.3 Mechanisms of particle acceleration in solar flares

The only source of charged particle acceleration that can increase their energy in comparison with the initial energy (for instance, the thermal one) is the work of the electric field done on a particle. In this case, significant acceleration can be achieved only when the rate of energy acquisition exceeds the rate of energy loss to collisions and radiation, which means that the accelerating field must, in a certain sense, be high.

Surprisingly, the consensus reached to date ends at this conclusion. It is evident that a fast restructuring of the magnetic field gives rise to a sufficiently high electric field, which may result in charged particle acceleration. But despite active theoretical research for many years, the roles of different specific acceleration mechanisms in the flares have not been fully elucidated. Nor is it quite clear yet whether a single 'universal' acceleration mechanism operates in the flares or different mechanisms can operate in different cases.

At present, two large groups of acceleration mechanisms are being considered: regular and stochastic. In the former case, acceleration is due to a regular electric field, for instance, in the vertical current sheet, postulated in the framework of the standard model [85–89], and the highest accelerated particle energies are determined by the field strength, the dimensions of the acceleration region, and the drift of the charged particles from this current sheet. The so-called betatron acceleration in a collapsing magnetic trap is a kind of regular acceleration [90, 91]. We note that regular mechanisms 'in pure form' permit the electrons to be accelerated to only relatively low energies ($\sim 10-100$ keV).

Stochastic acceleration mechanisms imply the presence of turbulence in one form or another, for instance, in the form of an ensemble of random waves, vortices, and/or pulsations. In this case, in the interaction between particles and waves, the energy transfer from waves to particles prevails on average, and their energy grows due to macroscopic perturbations [92, 93]. The stochastic mechanisms can include resonant [94, 95] as well as nonresonant acceleration [96–98]. These 'classical' mechanisms allow energy increase for electrons up to 1 MeV and higher. However, the acceleration time typically turns out to be too long, which contradicts the constraints that follow from observations. Stochastic acceleration can also occur in a strongly fragmented electric field not described by the superposition of separate magnetohydrodynamic or plasma waves [88, 99–103]. In this case, charged particles can be accelerated to high energies in subsecond time intervals [104].

Acceleration on a shock wave is regarded as a secondary mechanism of electron and ion acceleration. The acceleration of ions on a CME-driven shock wave is treated as the main mechanism for generation of high-energy SCRs registered in the interplanetary space at energies up to several GeV [105, 106].

2.4 Open questions in the physics of solar flares

It is noteworthy that the list of unsolved problems and open questions in solar flare physics is extremely long and is certainly not limited to the obvious incompleteness of the standard model [107]. In particular, it remains unclear where precisely the energy released during a flare is stored. How does a stable magnetic field transform into an unstable one and under what conditions does magnetic reconnection occur? Which is primary, the solar flare or the CME? What underlies the flare energy distribution among different components? Where are charged particles accelerated? What are the mechanisms of their acceleration? What is the maximum efficiency of particle acceleration and what is it determined by? What are the highest energies of the particles accelerated in solar flares?

Answering these questions invites the use of modern data with a high spatial and temporal resolution from all ranges of the electromagnetic spectrum, detailed theoretical investigations, and three-dimensional simulations. In this paper, we restrict ourselves primarily to the X-ray and gamma-ray ranges, which provide information mostly about nonthermal particles: their acceleration, transfer, and energy loss [108]. Next, we consider some issues related to the phenomenology and generation mechanisms of the high-energy emission of solar flares in more detail. An important role was here played by the results obtained by the joint Russia–US Konus-Wind space experiment.

3. Konus-Wind experiment

The Konus-Wind experiment has been performed by the Laboratory of Experimental Astrophysics of the Ioffe Institute since November 1994 up to the present with the Russian spectrometer Konus [47] aboard the GGS-Wind Space Observatory of the US National Aeronautics and Space Administration (NASA) (GGS: Global Geospace Science program). The main task of the experiment is the study of cosmic gamma-ray bursts [109, 110], soft gamma-ray repeaters (magnetars) [111, 112], solar flares, and other transient astrophysical phenomena in the hard X-ray and soft gamma-ray ranges.

The most important advantage of the Konus-Wind experiment is the location of the Wind spacecraft near the L1 point of the Sun–Earth system, at a distance of about 1.5 million km from Earth. This provides a stable background unaffected by the captured radiation zones and continuous all-sky observation without shading by Earth. The Konus-Wind spectrometer comprises two NaI(Tl) scintillation detectors with a broad range of recorded gamma-ray photons ($\sim$ 20 keV–15 MeV) and operates in two modes, the waiting and the triggered. In the waiting mode, continuously recorded photon count rates (temporal profiles) are available in three broad energy channels: G1 (20 – 80 keV), G2 (80 – 300 keV), and G3 (300–1200 keV), with a time resolution of 2.944 s. The triggered mode is intended for a detailed investigation of bright transient events. This mode involves recording the temporal emission profiles in the same channels, G1, G2, and G3 with a high resolution (up to 2 ms), along with recording multichannel spectra in the energy range 20 keV–15 MeV, which covers the emission range of electrons and ions accelerated in solar flares.

In the 25 years of continuous observations, over 1000 solar flares in the triggered mode and over 13,000 flares in the waiting mode have been registered in the Konus-Wind experiment. Konus-Wind is therefore a unique analogue of the GOES instrument, although operating in the hard X-ray range. The annual statistics of observations in the triggered mode for more than two complete cycles of solar activity are presented in Fig. 3. The temporal profiles and spectral data on all flares recorded in the triggered mode are publicly available on the website of the Ioffe Institute at http://www.ioffe.ru/LEA/kwsun/, and they are also available for direct loading via the Internet in the package OSPEX/SSW (Object Spectral Executive/Solar SoftWare).

Although a systematic analysis of the Konus-Wind data in the context of solar physics commenced relatively recently, these data enjoy wide use in the investigation of

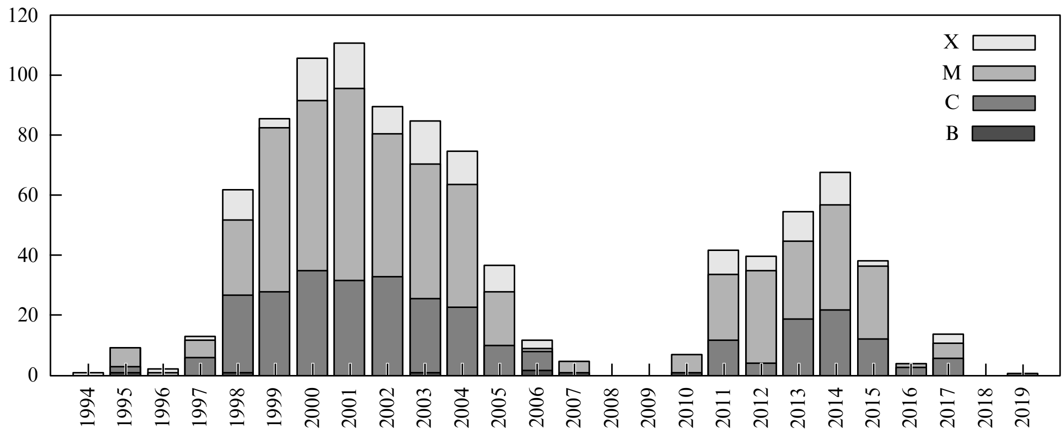

Figure 3. Annual distribution of the number of solar flares registered by Konus-Wind in the triggered mode.

X-ray and gamma-ray emission of solar flares [52, 53, 78, 113–121].

4. X-ray and gamma-ray emission of solar flares

4.1 X-ray emission spectrum of solar flares

The X-ray emission of solar flares is determined by deceleration of electrons in the solar atmosphere due to Coulomb losses. The emission of lower-energy thermal electrons is observed in the ultraviolet and soft X-ray ranges, and its parameters are determined by the temperature of electrons and their number, which measures the emission. Apart from the continuum generated due to the bremsstrahlung mechanism, the hot plasma radiates in atomic lines [122–124]. One of the brightest lines in the soft X-ray range is the line of the FeXXV/FeXX complex near an energy of 6.7 keV.

The bremsstrahlung of accelerated electrons lies in the hard X-ray and gamma-ray ranges. The shape of its spectrum is determined by the spectrum of injected electrons and the characteristics of the decelerating medium.

Usually, the spectra of nonthermal electrons are described well by different versions of a power-law spectrum, for instance, a single power law, a double power law with either a flattening or steepening at high energies, or power laws with a sharp cutoff above some energy. By and large, these phenomenological dependences are consistent with theoretical notions as well as particle acceleration and transfer models [92, 125, 126].

The relation between the electron power-law spectral index γ and the observed photon spectral index δ is determined by the conditions of bremsstrahlung generation, primarily by the energy fraction lost by the emitting electrons in the X-ray spectrum formation. Two limit cases are frequently considered: the 'thin target' and 'thick target' models. In the thin target model, nonthermal electrons lose only an insignificant part of their energy, and therefore the energy spectrum of the radiating electrons remains invariable and the photon spectral index is $\gamma_{\rm thin} = \delta + 1$ [127]. In the thick target model, nonthermal electrons are injected into a 'thick target' to lose all their energy in collisions. Because of the dependence of the Coulomb collision cross section on the incident electron energy, the nonthermal electron power-law spectral index in the thick target decreases by 2 in comparison with the power-law spectral index of electrons injected into the target. Accordingly, the power-law index of the photon spectrum is related to the spectral index of injected electrons as $\gamma_{\rm thick} = \delta - 1$ [128, 129].

Not infrequently, the hard X-ray flare spectrum is not described by a simple power law even for a single power-law spectrum of accelerated electrons [130]. The reason may lie with nonuniform ionization [131, the Compton albedo [132], or return current [83].

4.2 X-ray flare types

Based on the temporal, spectral, and spatial data of the Hinotory and SMM observatories, X-ray flares were conventionally divided into three types in Refs [133, 134]:

- type A: hot thermal flares observed at energies < 50 keV. Such flares are characterized by compact flare loops (< 5 Mm), smooth temporal profiles, and durations of the order of 10 min, whose nature is the thermal radiation of the heated plasma with a temperature up to 50 MK;
- type B: impulsive nonthermal flares with typical durations of each pulse of several dozen seconds. In this case, the flare loop dimensions are of the order of 20 Mm. For events of this type, hard X-ray radiation can be observed at energies as high as several hundred keV and characterized by the 'soft–hard–soft' spectral evolution. In Refs [135, 136], it was shown that this evolution is most likely a property of the acceleration mechanism itself rather than a consequence of particle propagation. A type-B flare registered in the Konus-Wind experiment is exemplified in Figs 4a–d;
- type C: gradual nonthermal flares with smoothly varying fluxes of hard X-ray and microwave radiation. Typical features of this flare type are complex systems of high (~ 50 Mm) loops and durations of the order of several dozen minutes [137–140]. The spectral evolution of hard X-ray radiation is described by the 'soft–hard–harder' law. Spectrum hardening with the progress of the flare is attributed to the capture of accelerated electrons in traps and the subsequent deceleration and scattering of lower-energy electrons into the loss cone (to thermal velocities) in combination with a smooth further acceleration of the more energetic ones [137, 139]. A type-C flare registered by the Konus-Wind experiment is exemplified in Figs 4e–h.

Type-A 'thermal' flares (whose examples can be found in Refs [141, 142]) supposedly result from direct coronal plasma heating by the energy released in magnetic reconnection, while in B- and C-type flares a significant part of the released magnetic energy is expended on particle acceleration. Of course, the existence of particle acceleration in the flare does not rule out direct plasma heating due to additional mechanisms. The most common flares are those in which the heating is effected both directly and by the energy loss of accelerated electrons [143] and possibly ions.

Two main components of thermal emission were singled out in Ref. [144]. The first is related to direct heating and is characterized by a higher temperature and a lower emission measure. The second component, which is characterized by a moderate temperature and a higher emission measure, stems from the effect of accelerated particles. It arises under the action of dynamic processes that comprise the hydrodynamic response of chromospheric and coronal plasmas to the flux of precipitating nonthermal electrons.

Although charged particle acceleration can coexist with 'direct' plasma heating, several events are described in the literature in which the bulk of the energy is expended on particle acceleration, while direct heating is absent or negligible. Such events were recently classified into a separate type [113], because in these events it is much easier to study the conversion of the released magnetic energy into other forms of energy. This type includes events in which significant nonthermal emission is attended by a relatively weak thermal response [53, 145–148], the so-called cold flares. An analysis of their energy budget suggests that the energy stored in accelerated electrons alone is sufficient for the observed plasma heating, without invoking direct heating mechanisms [149]. Studying cold flares makes it possible, first, to understand what underlies the energy distribution in a flare between thermal and nonthermal components and, second, to obtain a better estimate of the parameters of the nonthermal X-ray radiation at low energies ($\sim 5-20$ keV), because the admixture of thermal radiation at the impulsive phase is low for these events.

In Ref. [113] cold flares were systematically sought among the solar flares registered by Konus-Wind in the triggered

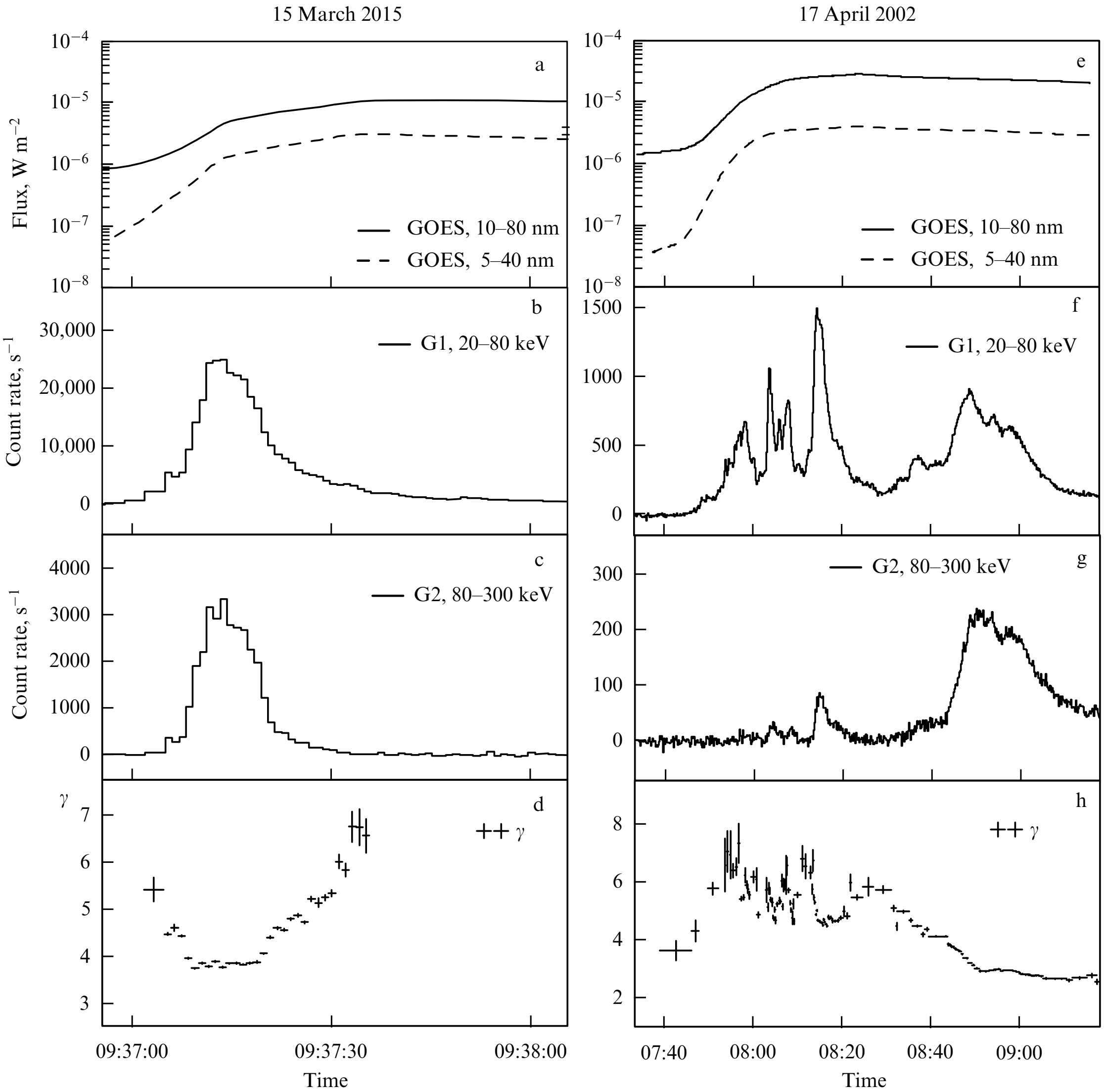

Figure 4. (a–d) Example of a type-B solar flare registered in the Konus-Wind experiment. (e–h) Example of a type-C solar flare registered in the Konus-Wind experiment. (a, e) Temporal profiles of soft X-ray radiation registered by the GOES instrument. (b, f) Temporal profiles of hard X-ray radiation in the G1 Konus-Wind channel. (c, g) Temporal profiles of hard X-ray radiation in the G2 Konus-Wind channel. (d, h) Power-law spectral indices of hard X-ray radiation estimated from Konus-Wind data.

mode in 1994–2017; the search was based on the ratio between the nonthermal (Konus-Wind) and thermal (GOES) emission fluxes. A statistical analysis of the selected events in the hard X-ray and microwave ranges revealed that some cold flares occur in compact dense loops with high magnetic fields, while the others are associated with low magnetic fields and tenuous plasmas. Both groups are nevertheless characterized by harder spectral indices than the 'average' flare. It remains unclear whether the harder spectra of cold flares are a feature of the acceleration process or are attributable to a selection effect. In the case of harder spectra, for instance, the precipitating electrons can penetrate into deeper layers of the solar atmosphere, which results in suppression of the chromospheric plasma evaporation. The resultant sample of flares dominated by nonthermal radiation will undoubtedly be extremely useful for detailed studies of particle acceleration mechanisms, the transfer of energy of accelerated particles to the thermal plasma, the thermal plasma evolution, and the dynamics of energy distribution in flares [149].

4.3 Constraints on particle acceleration mechanisms derived from hard X-ray observations

The hard X-ray emission of solar flares is observed on different time scales, from subsecond peaks to smooth hours-long events. It is still unclear whether different acceleration mechanisms are involved or long flares are superpositions of shorter ones [150].

The short peaks of hard X-ray emission can be treated as manifestations of short discrete acceleration episodes [151], whose duration is associated with the domain dimensions [152, 153] and the duration of reconnection [154]. Therefore, analyzing such 'elementary' bursts permits obtaining constraints on acceleration mechanisms.

An important acceleration parameter is the electric field strength, in particular, relative to the so-called Dreicer field [155]. The Dreicer field is the critical value of the external electric field whereby the electric Lorentz force is equilibrated by friction force for the majority of thermal-velocity electrons. In Coulomb collisions, the friction force is inversely proportional to the electron velocity squared [156]. For fields lower than the Dreicer field, 'sub-Dreicer' fields, only the fast particles in the tail of the Maxwell velocity distribution can experience acceleration. For fields higher than the Dreicer one, 'super-Dreicer' fields, the majority of particles undergo acceleration. The Dreicer field for electrons can be estimated as $E_{\mathrm{D}} \approx 10^{-8} n/T$ [V cm^{-1}] [156], where n is the plasma density in cm^{-3} and T is the plasma temperature in kelvins.

For typical plasma parameters in the acceleration region, the Dreicer field is $E_{\mathrm{D}} \sim 10^{-4}$ V cm^{-1}. We estimate the time τ required to accelerate an electron in this field to the characteristic energy of 0.5 MeV, using Newton's second law $\Delta\mathbf{p}/\Delta t = \mathbf{F}$. Ignoring the initial electron thermal velocity, we obtain $p/\tau = eE_{\mathrm{D}}$, where p is the relativistic momentum of the electron with an energy of 0.5 MeV and e is its charge, which gives the acceleration time $\tau \sim 300$ ms. This estimate confirms the fundamental importance of measuring the temporal structure and hard X-ray spectra with a resolution much better than 1 s provided by the triggered mode of the Konus-Wind experiment.

In recent study [78], estimates were made of the accelerating electric field strength and the temporal scale of acceleration in the M9.3 class flare, which occurred on August 4, 2011. Registered at the very onset of the impulsive phase of this event were subsecond peaks, which were observed both in the microwave range by the NoRP (Nobeyama Radio Polarimeters) radio telescope and in the hard X-ray range by Konus-Wind and Fermi-GBM experiments. Despite a high correlation of the temporal profiles measured in different ranges, delays of the order of several tens of milliseconds were observed among the hard X-rays at various energies (~ 20, ~ 50, ~ 100, ~ 200, and ~ 300 keV). These delays lie within 80 ms, and they are compatible with the delays arising from the time difference in the propagation from the loop top to the loop footpoints for electrons with different velocities. Because the time taken to accelerate electrons to higher energies is longer, the time scale of acceleration to the highest energies (~ 500 keV) observed in this flare should be appreciably shorter than the propagation delays and should therefore not exceed $\tau \sim 50$ ms. From the relation $p/\tau = eE$, we obtain the lower bound for the electric field strength $\sim 6 \times 10^{-4}$ V cm^{-1}, which is several times higher than the Dreicer field. Such fields and acceleration time scales are incompatible with stochastic mechanisms of acceleration by plasma turbulence, which imply acceleration times $\gtrsim 0.5$ s [157].

4.4 Gamma-ray emission of solar flares

4.4.1 Components of the solar flare spectrum in the gamma-ray range. The gamma-ray emission of solar flares, unlike their hard X-ray emission, is a superposition of several components [71, 158, 159]. It comprises the contributions both from ultrarelativistic electrons, which generate the bremsstrahlung continuum, and from accelerated ions, which are observed via the emission from the products of nuclear reactions in the solar atmosphere. The model gamma-ray spectrum of a solar flare is shown in Fig. 5.

In many cases, the bremsstrahlung continuum in the gamma-ray range can be described by a simple power law [38, 160]. At the same time, for some events, the continuum spectrum noticeably flattens at energies $\gtrsim 0.5-1$ MeV in comparison with its softer part [114, 161, 162]. In Ref. [161] this spectrum hardening is taken into account by introducing an additional component, a power-law function with an

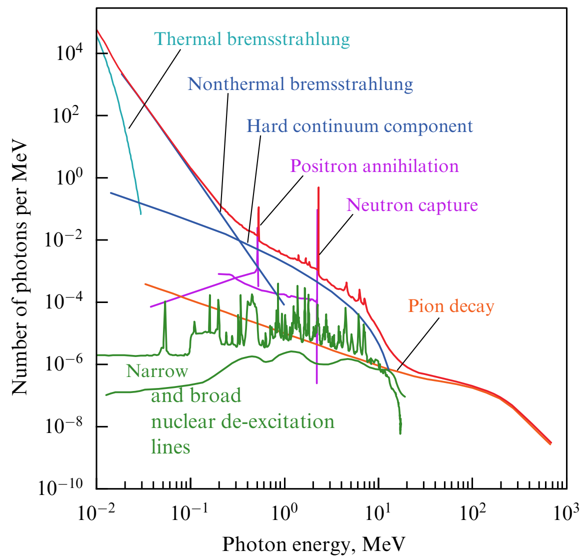

Figure 5. (Color online.) Example of the X-ray and gamma-ray emission spectrum of a solar flare: bremsstrahlung of thermal electrons (blue curve); two components of the hard X-ray continuum: the bremsstrahlung of nonthermal electrons and the hard component (dark blue); narrow and broad lines arising from the deexcitation of nuclei (green curves); radiation arising from electron–positron annihilation (purple curve); 2.223 MeV line arising from neutron capture by protons (purple curve); emission arising from pion decay (orange curve); the total spectrum (red curve). (Ronald Murphy, private communication.)

exponential decay in the high-energy domain, a cut-off power law (CPL) (see Fig. 5), while for the flares investigated in Refs [114, 162], the continuum was successfully described by a broken power law. The nature of continuum hardening remains a mystery. In Ref. [163], it was shown that it cannot be attributed to the propagation features of electrons but is presumably related to the features of their acceleration.

The dominant component of the gamma-ray solar flare spectrum in the energy range ~ 1–10 MeV is the superposition of characteristic lines arising from the nuclear reactions of accelerated ions. Gamma-ray lines from solar flares were first observed on August 4 and 7, 1973, by the OSO-7 spacecraft [164]. Emission due to 'direct' reactions is distinguished from emission due to 'inverse' reactions. In the former case, the incident particle is a proton or an alpha particle, while heavier ions are the targets. These reactions produce narrow lines with a full width at half-maximum (FWHM) $\sim 2\%$. The latter reactions, by contrast, occur between accelerated heavy ions and the protons or alpha particles of the ambient plasma. These reactions produce Doppler-broadened lines (FWHM$\sim 20\%$). The ratio between the fluxes in narrow and broad nuclear lines is a tool for investigating the elemental composition of the solar atmosphere and accelerated particles [165].

An important way to diagnose solar neutrons produced in nuclear reactions is the reaction of their capture with the production of deuterium $\mathrm{p} + \mathrm{n} \to {}^2\mathrm{H} + \gamma$, which is accompanied by a very narrow gamma line of 2.223 MeV. Because this reaction proceeds with the neutrons of thermal energy, the 2.223 MeV line is delayed by ~ 100 s relative to nuclear deexcitation lines, the time being required for the thermalization of neutrons [165–167].

The products of reactions of high-energy protons with other nuclei ($E \gtrsim 300$ MeV) are neutral, positive, and negative pions (π^0, π^+, π^-) [168, 169], among which positive pions prevail. Neutral pions decay into two gamma-ray photons with energies about 70 MeV in the pion rest frame and are observed in the spectrum in the form of a very broad peak. The decay of negative pions produces ultrarelativistic electrons, which in turn make a contribution to the bremsstrahlung continuum. The decay of positive pions gives rise to ultrarelativistic positrons. In addition to making a contribution to the bremsstrahlung, they can annihilate with electrons and produce either two gamma-ray photons with energies of 511 keV or three gamma-ray photons in the continuum with energies below 511 keV. The ratio between the 511 keV line and continuum fluxes permits estimating the conditions in the solar atmosphere, as was done in Ref. [170] from RHESSI data. Lower-energy positrons produced in the decay of β^+-active nuclei also contribute to the annihilation radiation, but the emission is delayed in this case [171, 172].

Because different energies are responsible for the generation of different components of gamma-ray emission, the ratio of their fluxes allows estimating the power-law spectral index of accelerated ions [165, 173] in the range from several MeV to several hundred MeV. In the high-energy range > 300 MeV, the spectral index can be estimated from the form of the pion decay spectrum [169].

4.4.2 Gamma-ray emission of the impulsive stage of the flare. Detailed investigations of the gamma-ray spectra of solar flares and their dynamics in combination with observations in softer ranges allow answering many questions related to the composition of the solar atmosphere as well as the mechanisms of electron and ion acceleration. The main difficulty stems from the relatively low fluxes of gamma-ray flare emission and, accordingly, long accumulation times of statistically significant spectral data.

The most complete catalog of solar flares accompanied by gamma-ray emission is presented in Ref. [174]. The catalog contains 258 flares, which were registered by the SMM/GRS instrument in 1980–1989 and demonstrated emission at energies > 300 keV. According to the data of the National Oceanic and Atmospheric Administration (NOAA),[1] about 23,000 flares of class C1.0 or higher were registered during this period, those with > 300 keV radiation accounting for $\sim 1\%$ of the flares. Gamma-ray lines were discovered in the spectra of 67 flares of these 258, which accounts for $\approx 0.3\%$ of the total number of flares of class C1.0 and higher. The results obtained in Ref. [174], as well as more recent results in Ref. [51] reliant on Fermi-LAT data, suggest that high-energy line emission is observed only in M- and X-class flares. The gamma radiation intensity nevertheless poorly correlates with the GOES flare class.

Based on Fermi-LAT data, reconstructing the spectral indices of accelerated protons at ~ 1 min intervals for the X8.2-class flare on September 10, 2017 suggested that protons with energies > 300 MeV of the impulsive phase of this flare are characterized by a temporal spectrum evolution from soft to hard and back (the 'soft–hard–soft' evolution type), with a repeated slight spectral hardening at the flare end [175]. The protons accelerated in the X10.0-class flare on October 29, 2003, according to the RHESSI and CORONAS-F/SONG data, exhibit the 'soft–hard–harder' type of spectral evolution [176]. These kinds of spectral evolutions are also characteristic of accelerated electrons (see Section 4.2), which testifies to the similarity of the acceleration and propagation processes for electrons and ions.

Among the ≈ 1000 flares registered over the 25 years of continuous observations by Konus-Wind in the triggered mode, which has permitted measuring multichannel spectra in the energy range 20 keV–15 MeV, only 93 events (1% of the total number) showed a significant flux at energies > 1 MeV, where gamma-ray lines play a significant role.

The observation of the impulsive phase of the X9.3-class flare on September 6, 2017 [114], which was the strongest flare of the 24th solar activity cycle, turned out to be one of the successes of the Konus-Wind experiment. This flare occurred when the RHESSI and Fermi spacecraft were in the shadow of Earth. A Bayesian analysis of the gamma-ray flare spectrum reliant on the Konus-Wind data revealed the presence of the continuum component, nuclear deexcitation lines, positron annihilation lines, and the neutron capture line, which is evidence of ion acceleration during the impulsive phase. The radiation continuum is described by a broken power law with a hardening in the high-energy part of the spectrum (see Section 4.4.1). The results of this analysis performed at time intervals of ~ 8 s are presented in Fig. 6. For the first time, the rapid spectral evolution of accelerated ions was revealed on a time scale of ~ 30 s, which repeated the spectral evolution of the bremsstrahlung continuum at low energies (< 300 keV), while the high-energy continuum exhibited a radically different evolution. Also for the first time, it was possible to measure the delay of the high-energy continuum relative to the low-energy one, which was ~ 17 s.

Based on the obtained relations between the continuum prior to and after the break, mechanisms can be proposed that are responsible for the appearance of the high-energy component. Due to its delay relative to the low-energy domain, it can hardly be ascribed to only the contribution of the electron–electron bremsstrahlung [177]. A possible reason for the high-energy part of the continuum with a harder spectral index may lie with the bremsstrahlung of ultrarelativistic positrons and electrons produced in the decay of charged pions. But in the current case, this is an unlikely scenario because the proton spectrum becomes softer as the flare develops, with the subsequent decrease in pion production, while the continuum intensity after the break, on the contrary, becomes higher. Secondary electron acceleration after the main flare peak, which somehow did not affect the ions, may be another reason. Lastly, one more explanation for the existence of the hard continuum component may lie in the admixture of emission generated by some other mechanism rather than the bremsstrahlung. Considered as a candidate for this mechanism is the inverse Compton photon scattering by high-energy electrons (G Share, private communication). But this explanation also runs into difficulties because this flare is characterized by a very strong coronal magnetic field [60], which should entail a rapid electron energy loss for gyrosynchrotron radiation.

4.4.3 Late-phase gamma-ray emission. In addition to the gamma-ray emission of the flare impulsive phase, extended late-phase gamma-ray emission was discovered, which follows the impulsive phase and can last from tens of

[1] These data are available at the site ftp://ftp.ngdc.noaa.gov/STP/space-weather/solar-data/solar-features/solar-flares/x-rays/goes/xrs.

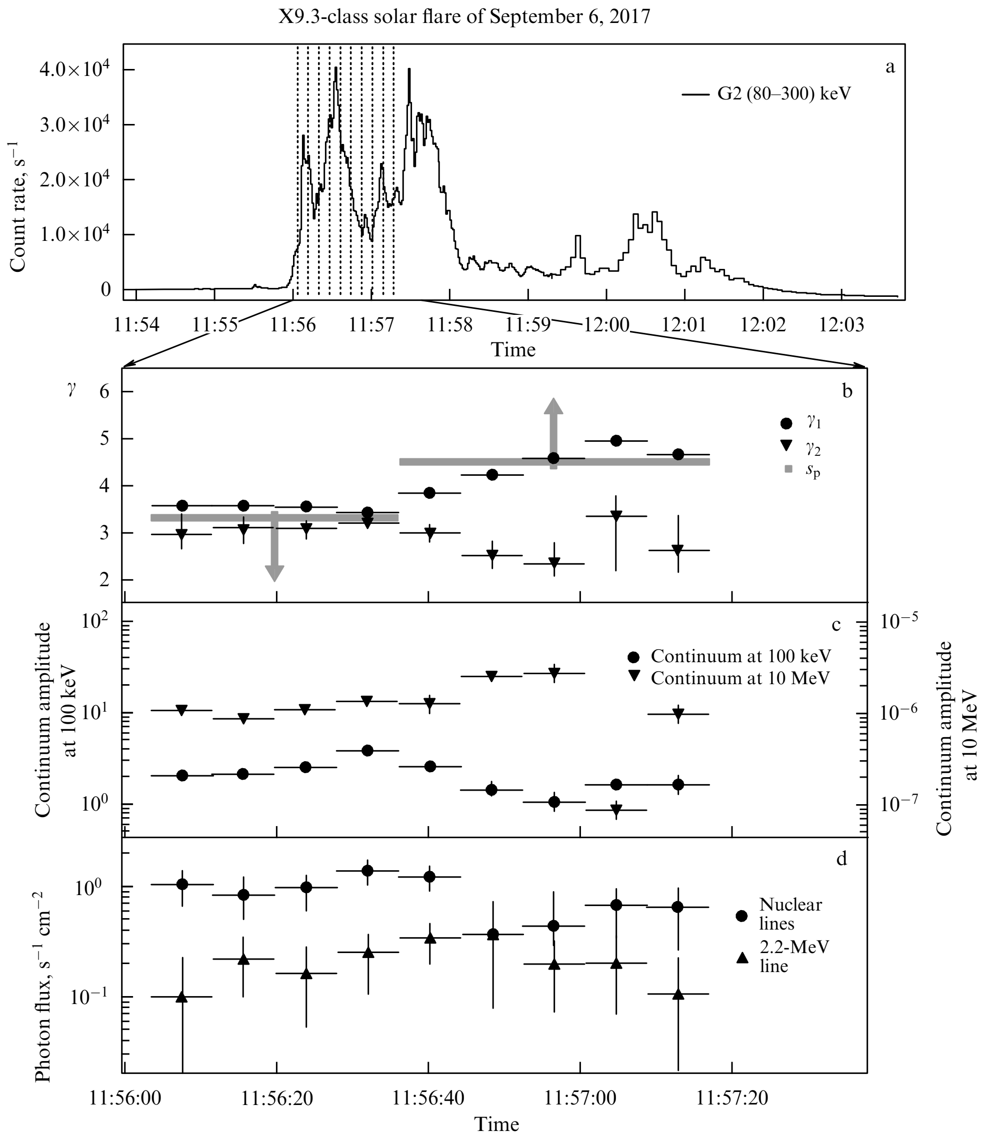

Figure 6. Observations of the X9.3-class solar flare on September 6, 2017 by the Konus-Wind instrument. (a) Temporal flare profile in the G2 channel; the vertical dotted lines show the time intervals in which the fitting was performed. (b) Evolution of the power-law spectral index of the continuum in the low-energy domain (dots), in the high-energy domain (triangles), and estimates of the power-law spectral index s_p for protons (grey lines). (c) Evolution of the continuum amplitude at 100 keV (dots) and 10 MeV (triangles). (d) Evolution of the flux due to nuclear deexcitation lines (dots) and 2.223 MeV neutron capture lines (triangles).

minutes to tens of hours [178]. A catalog of these events reliant on SMM data is presented in Ref. [179]. The late-phase spectrum, unlike the impulsive-phase spectrum, is nicely described by the pion decay emission [178]. The properties of late-phase gamma-ray emission of the 30 flares registered by the high-energy gamma-ray Fermi-LAT telescope were considered in a more recent paper [118]. It corroborated the conclusion about the prevalence of the pion component of emission, whose spectrum can extend to energies higher than 1 GeV. The late-phase emission can last up to 20 h. Furthermore, the majority of the events under discussion were attended by a fast CME ($V \gtrsim 800$ km s^{-1}).

One of the explanations for late-phase gamma-ray emission is the additional acceleration of protons on the shock wave of a fast CME (the Fermi mechanism of the first kind), which is similar to SCR acceleration but, unlike a SCR acceleration, is accompanied by backscattering and the subsequent return of protons to the Sun along open magnetic field lines [118]. This hypothesis explains both the delays of late-phase emission relative to the impulsive phase and its spectrum, but it also runs into difficulties. First, due to magnetic reflection, only a small fraction of accelerated protons can return to the solar atmosphere, where the magnetic field exceeds the CME field by several orders of magnitude. The 'lasso model' was proposed as a solution [180]: according to this model, the loop structure that holds the particles itself collapses to the solar surface. Second, revealed in Ref. [181] was the complete absence of correlation between the number of SCR protons and the number of protons required for the production of gamma-ray emission. Another possible explanation for late-phase gamma-ray emission is the additional proton acceleration in a magnetic trap by the Fermi mechanism of the second kind and subsequent diffusion in the higher-density photosphere [181, 182]. These issues are discussed in Section 4.5.3.

4.5 Spatial structure of hard X-ray and gamma-ray sources

Because hard X-ray and gamma-ray emission arises from the deceleration of accelerated electrons in a plasma and the nuclear reactions between accelerated ions and the ambient ions, the locations of the emission sources must correspond to domains 1) with a significant 'target' density, 2) with a significant density of accelerated particles, or 3) with a long-term interaction of the accelerated particles with the ambient medium. These conditions are respectively satisfied 1) in the footpoints of flare loops, 2) in particle acceleration domains, and 3) in the particle capture in traps.

4.5.1 Sources in loop footpoints and hot loops. The brightest hard X-ray sources are located in the highest-density plasma domains, the dense footpoints of flare loops [183] (see Fig. 2). Due to the heating by accelerated particles, the chromospheric plasma expands and gradually fills the flare (post-flare) loops, which begin to emit in the soft X-ray range [184]. These sources should be distinguished from the thermal sources at the loop tops, which frequently appear prior to the impulsive phase of a flare [79] and are associated with the pre-flare coronal plasma heating (see Section 4.2).

The positions of X-ray sources depend on the topology and dimensions of the flare loops. The source structure is not always resolved by the available instruments, and therefore closely located sources may be indistinguishable.

The most intense sources of impulsive gamma-ray emission are also located in the solar atmosphere at the loop footpoints. In Refs [185, 186], it was possible to obtain flare images at an energy of about 2.2 MeV, which corresponds to the neutron capture line. This energy is well suited for identifying the domains of ion interaction with the solar atmosphere: because the 2.2 MeV line is narrow, the admixture of continuum radiation is small and the bulk of the emission is produced in the interaction of protons with the solar atmosphere. The resultant data reveal the compactness of these gamma-ray sources and their proximity to the footpoints of flare loops. This suggests that the ions responsible for these sources were accelerated in the flare volume along with electrons.

At the same time, the positions of hard X-ray sources due to the deceleration of accelerated electrons in the plasma and the sources of gamma-ray emission at 2.2 MeV are offset relative to each other. The possible reasons for this offset are discussed in detail in Ref. [72]. Among them is the spatial separation of particles with opposite signs when accelerated by an electric field [185, 187].

4.5.2 Coronal sources. The coronal plasma is strongly rarefied in comparison to the photospheric one, and therefore the coronal sources are typically much weaker than the sources at the loop footpoints. Observing coronal sources becomes possible, for instance, when the loop footpoints are hidden by the solar limb (see, e.g., Refs [188–190]). This technique, which has received the name 'occultation technique,' remains topical with the advent of telescopes with a high spatial resolution, because their dynamic range does not always allow extracting the signal of a weak radiation source in the presence of a stronger one.

Coronal hard X-ray sources differ in origins and properties, and we consider some of their types below.

Coronal sources are frequently observed in the cusp region between the thermal loop and the point of magnetic reconnection (see Fig. 2). Such a source during the impulsive stage of the flare was first discovered from the Yohkoh data at energies of 23–53 keV [192]. Sources of this kind were termed Masuda sources. The cusp region corresponds to the area of the fastest magnetic field decay and hence of the most efficient acceleration and the highest density of accelerated particles [2].

Using the RHESSI data, about 120 sources at the loop top were selected with the help of the occultation technique [193, 194]. The hard X-ray emission in these cases is described sufficiently well by the thin target model. Observed for the hard and soft X-ray emission of coronal sources is the Neupert effect. For this flare sampling, we can therefore draw a conclusion about the similarity of the electron populations responsible for generating the radiation at the top and at the footpoints of a flare loop.

There are flares [195–197] in which X-ray emission is distributed over the entire flare loop or over a large part of it. In this case, the sources in the loop footpoints are hardly present or are very weak. This signifies that accelerated electrons, in propagating through the loop, lose a significant part of their energy in the corona without reaching the footpoints. The fast energy loss of nonthermal electrons is explained by the high density of flare loops in these events. The presence of nonthermal electrons in the dense flare loops implies that their acceleration occurs directly in the volume of these dense loops [198–200].

Hard X-ray and gamma-ray emission in the corona can also be produced by the accelerated particles captured in magnetic traps. Such sources can reside in flare loops [201] as well as in coronal mass ejections [202, 203]. In this case, the power-law index of the photon spectrum often hardens in the course of the flare development (see Section 4.2). This issue is addressed in Section 4.5.4.

4.5.3 Remote sources. Sometimes, X-ray and gamma-ray sources are observed on the solar disk very far, up to several dozen degrees of longitude, from the active region that gives rise to the solar flare [190, 204]. This emission can be caused by the diffusion of charged particles high in the corona along open magnetic field lines and their subsequent return to the Sun, but outside the initial acceleration region. The initial appearance of such particles in the corona may be due to their escape from a magnetic trap, similar to that described in Ref. [203], or to the additional particle acceleration at the broad shock front of a CME [204]. The existence of a spatially extended component was first proposed to explain the anomalously strong emission at the 2.2 MeV neutron capture line observed from the flare of September 29, 1989 [190], which was behind the solar limb.

The emission of remote sources can be regarded as a more general case of late-phase gamma-ray emission (see Section 4.4.3), which can be caused not only by accelerated protons but also by electrons. The emission from diffusing particles can be weak and, by analogy with weak sources in the corona, can be observed only with the shading of more intense sources, i.e., in the case of partially occulted or behind-the-limb flares.

4.5.4 Behind-the-limb flares. In some cases, hard X-ray sources reside very high in the corona, at altitudes of ~ 100 Mm, which makes it possible to observe the emission of flares whose footpoints are hidden behind the solar limb

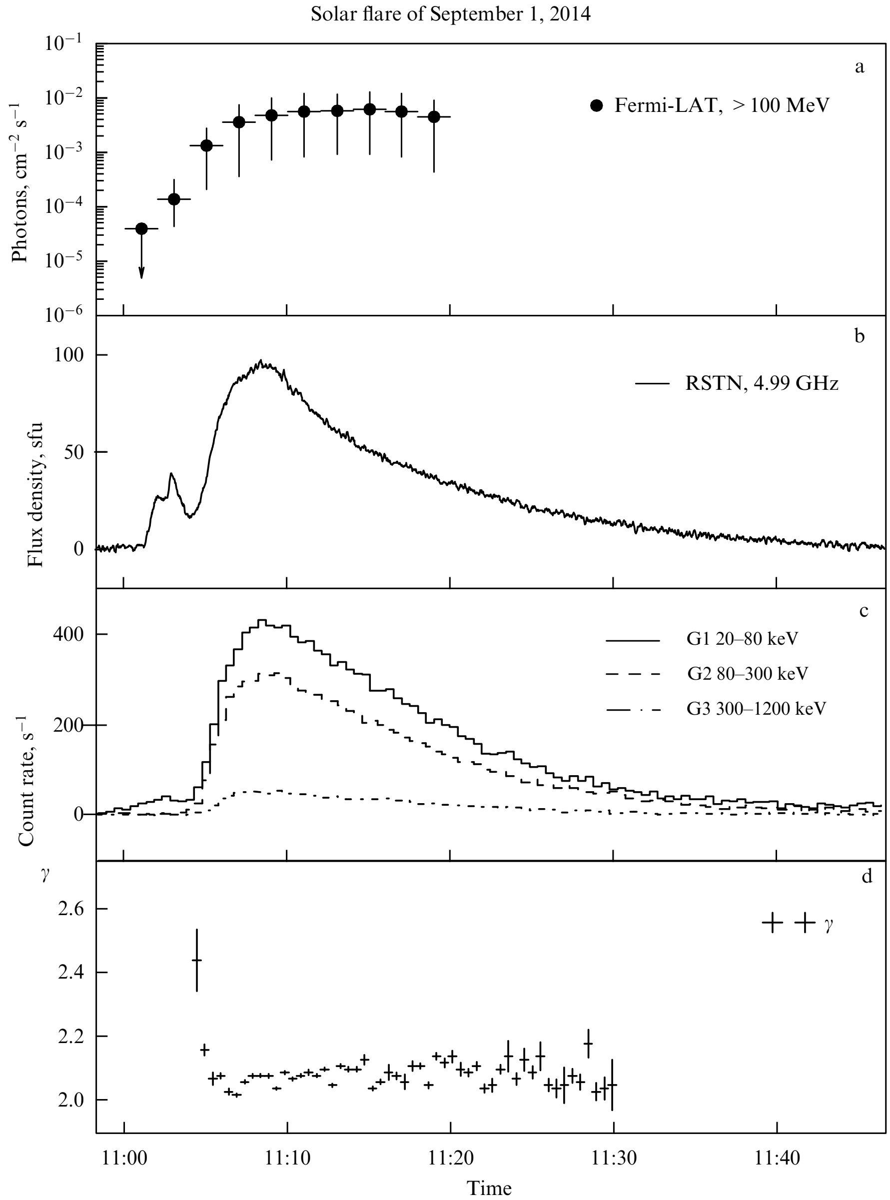

Figure 7. Observations of the behind-the-limb flare of September 1, 2017. (a) Temporal profile of the radiation fluxes with energies above 100 MeV according to the Fermi-LAT instrument data. (b) Temporal profile in the microwave range at a frequency of 4.99 GHz according to the RSTN data (sfu: solar flux unit, 1 sfu = 10^4 Jy). (c) Temporal profiles of hard X-ray radiation according to the Konus-Wind data in G1, G2, and G3 channels. (d) Evolution of the hard X-ray photon power-law spectral index estimated from measurements in the G1, G2, and G3 channels.

and are at longitudes up to $\sim 45°$ (see, e.g., Ref. [189]), the so-called behind-the-limb flares. The borderline between the terms 'behind-the-limb' and 'partially occulted' flares is rather blurred and the difference between them is that behind-the-limb flares occur rather far behind the limb, unlike partially occulted ones.

Behind-the-limb flares offer good opportunities for observing weak and poorly studied emission components. Unfortunately, these opportunities are quite infrequent: not many more than ten behind-the-limb events have been described during the entire observation period.

One of the first registered behind-the-limb flares was the famous Frost–Dennis event [205]: a short impulsive peak was followed by a second maximum about 20 min in duration, characterized by a peculiar smooth temporal profile. The second stage of electron acceleration by the Fermi mechanism of the first kind on a shock wave was proposed as an explanation of this smooth maximum [206]. More recently, several more behind-the-limb flares with similar characteristics have been discovered [188, 207]. In addition to the smooth temporal profile, these events were characterized by very hard X-ray spectra and a nearly complete absence of spectral evolution, which strikingly distinguishes them from 'typical' flares on the solar disk, shown in Fig. 4.

Observations of the X-ray sources of behind-the-limb flares by Yohkoh and RHESSI telescopes [202, 203] with spatial resolution resulted in the idea that hard X-ray emission is produced by the electrons that propagate after acceleration upwards from the solar surface [208] and enter a magnetic trap behind the CME front.

Furthermore, hard X-ray [191, 209] and gamma-ray [52] emission of behind-the-limb flares can be related to remote sources (see Section 4.5.3). In this case, the particles captured in a high trap diffuse along the magnetic field lines and return to the side of the Sun visible to a terrestrial observer.

A new surge of interest in behind-the-limb flares was generated by the flare of September 1, 2014 discovered in waiting-mode observations of the Konus-Wind. The locations of the loop footpoints of this flare were estimated using the STEREO-B (Solar Terrestrial Relations Observatory) space observatory. They were located at a longitude of about 45° behind the limb [52]. The coronal source was observed not only by the Konus-Wind instrument but also by the Fermi-LAT gamma-ray telescope at energies above 100 MeV from a near-Earth orbit and by the Radio Solar Telescope Network (RSTN) on the ground in the microwave range [52]. The temporal profiles of the event and the variations in the power-law spectral index of the photon spectrum are shown in Fig. 7 with a high degree of correlation of the temporal profiles in the gamma-ray, hard X-ray, and microwave ranges. At the same time, the hard X-ray spectrum, as in the case of events presented in Refs [188, 207], does not vary in the course of the flare and is characterized by a photon power-law spectral index close to 2, which is the limit hard value for a bremsstrahlung spectrum.

This flare led to extensive discussions about the origin of X-ray and gamma-ray emission (see, e.g., Refs [52, 116, 209, 210]). The issues under discussion are the existence of a second acceleration stage and the mechanisms involved in this case, the possible differences between the spectra of electrons propagating upwards and downwards from the acceleration region, as well as the propagation features of electrons and protons in the corona.

Stereoscopic observations of solar flares [116, 189, 208, 211] are a great help in the search for answers to these questions. At present, stereoscopic observations in the hard X-ray range are possible, in particular, involving data from the domestic High-Energy Neutron Detector (HEND) experiment aboard the Mars-Odyssey SC in a near-Mars orbit [212, 213]. They provide unique information about the event phase invisible from Earth.

It is not known whether behind-the-limb flares comprise a uniform class of events or several subgroups with different particle acceleration mechanisms, features of particle propagation, and emission. Because the observations of behind-the-limb flares are infrequent and scattered, an analysis of their statistically significant sampling has never been undertaken.

The waiting-mode data of the Konus-Wind experiment offer a unique possibility for the retrospective search for behind-the-limb flares for more than two complete solar cycles. This search, involving the data from GOES in the soft X-ray range, radio observatories in the microwave range, and telescopes with high spatial resolution, was carried out using the Konus-Wind data of 1994–2019 (Lysenko et al., in preparation). It was possible to find 20 flares with loop footpoints located at longitudes from 8° to 40° behind the limb, including four previously known events [52, 202, 203, 211]. Figure 8 shows the footpoint positions, on the far side of the Sun, of the found behind-the-limb flares. This selection does not contain behind-the-limb events comparable in intensity to the flare of September 1, 2014 described above.

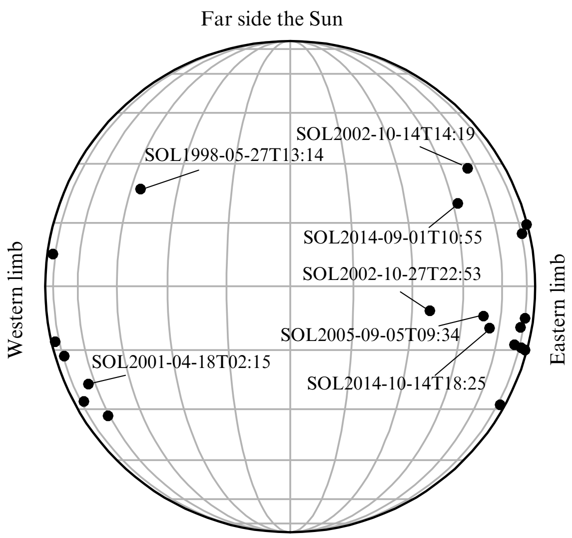

Figure 8. Positions of the loop footpoints on the far side of the Sun for 20 behind-the-limb flares discovered in the retrospective search using Konus-Wind data. Indicated are several flares known from previous observations, whose loop footpoints are far behind the limb.

5. Conclusions

Owing to the tremendous progress in observational methods in astrophysics, a general picture of the processes occurring in solar flares has taken shape in the past decades. However, many problems remain to be solved on the path to constructing a self-consistent physical model of solar flares.

Among them, for instance, are specific mechanisms of particle acceleration in the volume of a flare itself as well as of the possible subsequent acceleration in the corona, the energy distribution among the flare components, the relation between the solar flares, solar cosmic rays, and CMEs, the propagation of particles in the corona, and the similarities and differences between the acceleration of electrons and ions.

The answers to these questions may be provided by multiwavelength observations with high spatial, temporal, and energy resolution, in combination with theoretical research and simulations.

At present, solar observations in the high-energy part of the spectrum are at a tipping point. On the one hand, the RHESSI observatory, which was the key instrument for solar research in the X-ray and soft gamma-ray ranges for a long time, stopped its operations in September 2018. On the other hand, the operation of the Fermi, INTEGRAL, and Wind observatories continues, and the scientific community expects the arrival of new X-ray observational data from the new Solar Orbiter (SolO) mission [214], as well as of X-ray and gamma-ray data from the Intergeliozond mission [215] under preparation. The launch of these observatories will permit solar astrophysics to reach a new level, that of regular stereoscopic observations.

In the future, a breakthrough in solar research would be provided by an instrument capable of X-ray and gamma-ray imaging with a high spatial resolution combined with a good spectral resolution and a broad dynamic range. The development and launch of such a telescope is a challenge for the coming decades.

References

1. Somov B V *Phys. Usp.* **53** 954 (2010); *Usp. Fiz. Nauk* **180** 997 (2010)
2. Fleishman G D et al. *Science* **367** 278 (2020)
3. Clarke J T et al. *Nature* **433** 717 (2005)
4. Hesse M, Forbes T G, Birn J *Astrophys. J.* **631** 1227 (2005)
5. Schrijver C J, Title A M *Astrophys. J.* **597** L165 (2003)
6. Belenkaya E S *Phys. Usp.* **52** 765 (2009); *Usp. Fiz. Nauk* **179** 809 (2009)
7. Bhattacharjee A *Annu. Rev. Astron. Astrophys.* **42** 365 (2004)
8. Yi Y, Caputo F M, Brandt J C *Planet. Space Sci.* **42** 705 (1994)
9. Gosling J T et al. *J. Geophys. Res.* **110** A01107 (2005)
10. Safargaleev V V et al. *Phys. Usp.* **58** 612 (2015); *Usp. Fiz. Nauk* **185** 655 (2015)
11. Thompson C *Mon. Not. R. Astron. Soc.* **270** 480 (1994)
12. Granot J *Astrophys. J. Lett.* **816** L20 (2016)
13. Aptekar R L et al. *Phys. Usp.* **62** 739 (2019); *Usp. Fiz. Nauk* **189** 785 (2019)
14. Sofue Y, Kigure H, Shibata K *Publ. Astron. Soc. Jpn.* **57** L39 (2005)
15. de Gouveia Dal Pino E M, Lazarian A *Astron. Astrophys.* **441** 845 (2005)
16. Tanuma S et al. *Publ. Astron. Soc. Jpn.* **51** 161 (1999)
17. Schopper R, Lesch H, Birk G T *Astron. Astrophys.* **335** 26 (1998)
18. Ptitsyna K V, Troitsky S V *Phys. Usp.* **53** 691 (2010); *Usp. Fiz. Nauk* **180** 723 (2010)
19. Thompson C, Duncan R C *Astrophys. J.* **561** 980 (2001)
20. Hurley K et al. *Nature* **434** 1098 (2005)
21. Dokuchaev V I, Eroshenko Yu N *Phys. Usp.* **58** 772 (2015); *Usp. Fiz. Nauk* **185** 829 (2015)
22. Donati J-F et al. *Mon. Not. R. Astron. Soc.* **345** 1145 (2003)
23. Donati J-F et al. *Mon. Not. R. Astron. Soc.* **390** 545 (2008)
24. Marsden S C et al. *Mon. Not. R. Astron. Soc.* **413** 1922 (2011)
25. Garraffo C et al. *Astrophys. J. Lett.* **843** L33 (2017)
26. Wood B E *J. Phys. Conf. Ser.* **1100** 012028 (2018)
27. Drake J J et al. *Astrophys. J.* **764** 170 (2013)
28. Van Doorsselaere T, Kupriyanova E G, Yuan D *Solar Phys.* **291** 3143 (2016)
29. Solanki S K et al. *Nature* **431** 1084 (2004)
30. Hathaway D H *Living Rev. Solar Phys.* **12** 4 (2015)
31. Carrington R C *Mon. Not. R. Astron. Soc.* **20** 13 (1859)
32. Hey J S *Nature* **157** 47 (1946)
33. Mandel'shtam S L et al. *Planet. Space Sci.* **11** 61 (1963)
34. Friedman H *Annu. Rev. Astron. Astrophys.* **1** 59 (1963)
35. Zhitnik I A et al. *Cosmic Res.* **5** 237 (1967)
36. Chipman E G *Astrophys. J.* **244** L113 (1981)
37. Lin R P et al. *Solar Phys.* **210** 3 (2002)
38. Lin R P et al. *Astrophys. J.* **595** L69 (2003)
39. Sui L, Holman G D *Astrophys. J.* **596** L251 (2003)
40. Lin J et al. *Astrophys. J.* **622** 1251 (2005)
41. Sui L, Holman G D, Dennis B R *Astrophys. J.* **612** 546 (2004)
42. Krucker S et al. *Astrophys. J.* **714** 1108 (2010)
43. Kiplinger A L et al. *Astrophys. J.* **265** L99 (1983)
44. Akimov V V et al. *AIP Conf. Proc.* **294** 130 (1994)
45. Kuznetsov S N et al. *Solar Syst. Res.* **40** 104 (2006); *Astron. Vest.* **40** 120 (2006)
46. Pal'shin V D et al. *Geomagn. Aeron.* **54** 943 (2014)
47. Aptekar R L et al. *Space Sci. Rev.* **71** 265 (1995)
48. Meegan C et al. *Astrophys. J.* **702** 791 (2009)
49. Atwood W B et al. *Astrophys. J.* **697** 1071 (2009)
50. Winkler C et al. *Astron. Astrophys.* **411** L1 (2003)
51. Ackermann M et al. *Astrophys. J.* **787** 15 (2014)
52. Ackermann M et al. *Astrophys. J.* **835** 219 (2017)
53. Fleishman G D et al. *Astrophys. J.* **822** 71 (2016)
54. Kiener J et al. *Astron. Astrophys.* **445** 725 (2006)
55. Shibata K et al. *Astrophys. J. Lett.* **451** L83 (1995)
56. Gary G A *Solar Phys.* **203** 71 (2001)
57. Zirin H, Wang H *Nature* **363** 426 (1993)
58. Guo Y et al. *Astrophys. J.* **679** 1629 (2008)
59. Wang H et al. *Res. Notes Am. Astron. Soc.* **2** (1) 8 (2018)
60. Anfinogentov S A et al. *Astrophys. J. Lett.* **880** L29 (2019)
61. Kuridze D et al. *Astrophys. J.* **860** 10 (2018)
62. Brosius J W, White S M *Astrophys. J.* **641** L69 (2006)
63. Carmichael H, in *The Physics of Solar Flares, Proc. of the AAS-NASA Symp., 28–30 October, 1963, Greenbelt, MD, USA* (NASA Special Publ., Vol. 50, Ed. W N Hess) (Washington, DC: National Aeronautics and Space Administration, Science and Technical Information Division, 1964) p. 451
64. Sturrock P A *Nature* **211** 695 (1966)
65. Kopp R A, Pneuman G W *Solar Phys.* **50** 85 (1976)
66. Hirayama T *Solar Phys.* **34** 323 (1974)
67. Reames D V *Space Sci. Rev.* **90** 413 (1999)
68. Bruno A et al. *Astrophys. J.* **862** 97 (2018)
69. Lin R P *Space Sci. Rev.* **86** 61 (1998)
70. Mewaldt R A et al. *J. Geophys. Res.* **110** A09S18 (2005)
71. Ramaty R, Kozlovsky B, Lingenfelter R E *Space Sci. Rev.* **18** 341 (1975)
72. Vilmer N, MacKinnon A L, Hurford G J *Space Sci. Rev.* **159** 167 (2011)
73. Mel'nikov V F *Radiophys. Quantum Electron.* **37** 557 (1994); *Izv. Vyssh. Uchebn. Zaved. Radiofiz.* **37** 856 (1994)
74. Neupert W M *Astrophys. J.* **153** L59 (1968)
75. Kundu M R *Adv. Space Res.* **4** (7) 157 (1984)
76. Nishio M et al. *Astrophys. J.* **489** 976 (1997)
77. Hanaoka Y *Solar Phys.* **173** 319 (1997)
78. Altyntsev A T et al. *Astrophys. J.* **883** 38 (2019)
79. Benz A O *Living Rev. Solar Phys.* **5** (1) 1 (2008)
80. Brown J C, Emslie A G *Astrophys. J.* **331** 554 (1988)
81. Knight J W, Sturrock P A *Astrophys. J.* **218** 306 (1977)
82. Diakonov S V, Somov B V *Solar Phys.* **116** 119 (1988)
83. Zharkova V V, Gordovskyy M *Astron. Astrophys.* **432** 1033 (2005)
84. Emslie A G et al. *Astrophys. J.* **759** 71 (2012)
85. Litvinenko Y E, Somov B V *Sov. Astron. Lett.* **17** 353 (1991); *Pis'ma Astron. Zh.* **17** 835 (1991)
86. Litvinenko Yu E, Somov B V *Solar Phys.* **146** 127 (1993)
87. Benka S G, Holman G D *Astrophys. J.* **435** 469 (1994)
88. Gordovskyy M, Browning P K *Astrophys. J.* **729** 101 (2011)
89. Vlahos L, Isliker H *Plasma Phys. Control. Fusion* **61** 014020 (2019)
90. Somov B V, Kosugi T *Astrophys. J.* **485** 859 (1997)
91. Grady K J, Neukirch T, Giuliani P *Astron. Astrophys.* **546** A85 (2012)
92. Aschwanden M J *Physics of the Solar Corona. An Introduction with Problems and Solutions* 2nd ed. (Berlin: Springer, 2006)
93. Zharkova V V et al. *Space Sci. Rev.* **159** 357 (2011)
94. Pryadko J M, Petrosian V *Astrophys. J.* **482** 774 (1997)
95. Petrosian V, Liu S *Astrophys. J.* **610** 550 (2004)
96. Miller J A, Larosa T N, Moore R L *Astrophys. J.* **461** 445 (1996)
97. Bykov A M, Fleishman G D *Astrophys. J.* **692** L45 (2009)
98. Fleishman G D, Toptygin I N *Mon. Not. R. Astron. Soc.* **429** 2515 (2013)
99. Drake J F et al. *Nature* **443** 553 (2006)
100. Turkmani R et al. *Astrophys. J.* **620** L59 (2005)
101. Turkmani R et al. *Astron. Astrophys.* **449** 749 (2006)
102. Cargill P J et al. *Space Sci. Rev.* **173** 223 (2012)
103. Gordovskyy M, Browning P K *Solar Phys.* **277** 299 (2012)
104. Isliker H, Archontis V, Vlahos L *Astrophys. J.* **882** 57 (2019)
105. Aschwanden M J *Space Sci. Rev.* **171** 3 (2012)
106. Reames D V *Astrophys. J.* **757** 93 (2012)
107. Fletcher L et al. *Space Sci. Rev.* **159** 19 (2011)
108. Holman G D et al. *Space Sci. Rev.* **159** 107 (2011)
109. Racusin J L et al. *Nature* **455** 183 (2008)
110. Tsvetkova A et al. *Astrophys. J.* **850** 161 (2017)
111. Mazets E P et al. *Astron. Lett.* **25** 635 (1999); *Pis'ma Astron. Zh.* **25** 735 (1999)
112. Frederiks D D et al. *Astron. Lett.* **33** 1 (2007); *Pis'ma Astron. Zh.* **33** (2007)
113. Lysenko A L et al. *Astrophys. J.* **856** 111 (2018)
114. Lysenko A L et al. *Astrophys. J.* **877** 145 (2019)
115. Sharykin I N, Kosovichev A G *Astrophys. J.* **864** 86 (2018)
116. Grechnev V V et al. *Solar Phys.* **293** 133 (2018)
117. Glesener L, Fleishman G D *Astrophys. J.* **867** 84 (2018)
118. Share G H et al. *Astrophys. J.* **869** 182 (2018)
119. Altyntsev A et al. *Solar Phys.* **291** 445 (2016)
120. Altyntsev A et al. *Solar Phys.* **292** 137 (2017)
121. Li D et al. *Astrophys. J.* **888** 53 (2020)
122. Dere K P et al. *Astron. Astrophys. Suppl. Ser.* **125** 149 (1997)

123. White S M, Thomas R J, Schwartz R A *Solar Phys.* **227** 231 (2005)
124. Phillips K J H, Feldman U, Landi E *Ultraviolet and X-ray Spectroscopy of the Solar Atmosphere* (Cambridge: Cambridge Univ. Press, 2012)
125. Oka M et al. *Space Sci. Rev.* **214** 82 (2018)
126. Isliker H, Vlahos L, Constantinescu D *Phys. Rev. Lett.* **119** 045101 (2017)
127. Tandberg-Hanssen E, Emslie A G *The Physics of Solar Flares* (Cambridge: Cambridge Univ. Press, 1988)
128. Brown J C *Solar Phys.* **18** 489 (1971)
129. Somov B V, Syrovatskii S I *Sov. Phys. Usp.* **19** 813 (1976); *Usp. Fiz. Nauk* **120** 217 (1976)
130. Kontar E P et al. *Space Sci. Rev.* **159** 301 (2011)
131. Kontar E P, Brown J C, McArthur G K *Solar Phys.* **210** 419 (2002)
132. Kontar E P et al. *Astron. Astrophys.* **446** 1157 (2006)
133. Tanaka K et al. *Solar Phys.* **86** 91 (1983)
134. Dennis B R *Solar Phys.* **100** 465 (1985)
135. Grigis P C, Benz A O *Astron. Astrophys.* **426** 1093 (2004)
136. Battaglia M, Benz A O *Astron. Astrophys.* **456** 751 (2006)
137. Cliver E W et al. *Astrophys. J.* **305** 920 (1986)
138. Kiplinger A L *Astrophys. J.* **453** 973 (1995)
139. Grigis P C, Benz A O *Astrophys. J.* **683** 1180 (2008)
140. Grayson J A, Krucker S, Lin R P *Astrophys. J.* **707** 1588 (2009)
141. Gary D E, Hurford G J *Astrophys. J.* **339** 1115 (1989)
142. Fleishman G D, Nita G M, Gary D E *Astrophys. J.* **802** 122 (2015)
143. Veronig A et al. *Astron. Astrophys.* **392** 699 (2002)
144. Warmuth A, Mann G *Astron. Astrophys.* **588** A115 (2016)
145. White S M et al. *Astrophys. J.* **384** 656 (1992)
146. Bastian T S, Fleishman G D, Gary D E *Astrophys. J.* **666** 1256 (2007)
147. Fleishman G D et al. *Astrophys. J. Lett.* **731** L19 (2011)
148. Masuda S et al. *Publ. Astron. Soc. Jpn.* **65** (sp1) S1 (2013)
149. Motorina G G, Fleishman G D, Kontar E P *Astrophys. J.* **890** 75 (2020)
150. Lu E T, Hamilton R J *Astrophys. J. Lett.* **380** L89 (1991)
151. Kane S R et al. *Astrophys. J.* **271** 376 (1983)
152. Sturrock P A et al. *Solar Phys.* **94** 341 (1984)
153. Larosa T N, Moore R L *Astrophys. J.* **418** 912 (1993)
154. Litvinenko Yu E *Solar Phys.* **167** 321 (1996)
155. Dreicer H *Phys. Rev.* **115** 238 (1959)
156. Trubnikov B A, in *Reviews of Plasma Physics* Vol. 1 (Ed. M A Leontovich) (New York: Consultants Bureau, 1965) p. 105; Translated from Russian: *Voprosy Teorii Plazmy* Vol. 1 (Ed. M A Leontovich) (Moscow: Gosatomizdat, 1963) p. 98
157. Chen Q, Petrosian V *Astrophys. J.* **777** 33 (2013)
158. Dolan J F, Fazio G G *Rev. Geophys.* **3** 319 (1965)
159. Kuzhevskii B M *Sov. Astron.* **12** 595 (1969); *Astron. Zh.* **45** 747 (1968)
160. Share G H, Murphy R J, in *High Energy Solar Physics Workshop — Anticipating HESSI* (ASP Conf. Ser., Vol. 206, Eds R Ramaty, N Mandzhavidze) (Bristol: IOP Publ., 2000) p. 377
161. Ackermann M et al. *Astrophys. J.* **745** 144 (2012)
162. Share G H et al. *Astrophys. J.* **595** L85 (2003)
163. Petrosian V, McTiernan J M, Marschhauser H *Astrophys. J.* **434** 747 (1994)
164. Chupp E L et al. *Nature* **241** 333 (1973)
165. Murphy R J et al. *Astrophys. J. Suppl.* **168** 167 (2007)
166. Prince T A et al., in *Proc. from the 18th Intern. Cosmic Ray Conf., Bangalore, India, 22 August – 3 September, 1983* Vol. 4 (Eds N Durgaprasad et al.) (Bombay: Tata Institute of Fundamental Research, 1983) p. 79
167. Shih A Y, Lin R P, Smith D M *Astrophys. J.* **698** L152 (2009)
168. Crannell C J, Crannell H, Ramaty R *Astrophys. J.* **229** 762 (1979)
169. Murphy R J, Dermer C D, Ramaty R *Astrophys. J. Suppl.* **63** 721 (1987)
170. Murphy R J et al. *Astrophys. J. Suppl.* **161** 495 (2005)
171. Crannell C J et al. *Astrophys. J.* **210** 582 (1976)
172. Kozlovsky B, Lingenfelter R E, Ramaty R *Astrophys. J.* **316** 801 (1987)
173. Hua X-M, Lingenfelter R E *Solar Phys.* **107** 351 (1987)
174. Vestrand W T et al. *Astrophys. J. Suppl.* **120** 409 (1999)
175. Omodei N et al. *Astrophys. J.* **865** L7 (2018)
176. Kurt V G et al. *New Astron.* **56** 102 (2017)
177. Kontar E P et al. *Astrophys. J.* **670** 857 (2007)
178. Forrest D J et al., in *Proc. from the 19th Intern. Cosmic Ray Conf., La Jolla, USA, August 11 – 23, 1985* (NASA Conf. Publ., NASA CP-2376, Vol. 4, Eds F C Jones, J Adams, G M Mason) (Washington, DC: NASA, 1985) p. 146
179. Ryan J M *Space Sci. Rev.* **93** 581 (2000)
180. Hudson H S, in *Space Weather of the Heliosphere: Processes and Forecasts, Proc. IAU Symp., S335* (Proc. IAU Symp., Vol. 13, Eds C Foullon, O E Malandraki) (Cambridge: Cambridge Univ. Press, 2018) p. 49
181. de Nolfo G A et al. *Astrophys. J.* **879** 90 (2019)
182. Ryan J M, Lee M A *Astrophys. J.* **368** 316 (1991)
183. Hoyng P et al. *Astrophys. J.* **246** L155 (1981)
184. Antiochos S K, Sturrock P A *Astrophys. J.* **220** 1137 (1978)
185. Hurford G J et al. *Astrophys. J.* **595** L77 (2003)
186. Hurford G J et al. *Astrophys. J.* **644** L93 (2006)
187. Fleishman G D, Toptygin I N *Cosmic Electrodynamics: Electrodynamics and Magnetic Hydrodynamics of Cosmic Plasmas* (Astrophysics and Space Science Library, Vol. 388) (New York: Springer, 2013)
188. Hudson H S, Lin R P, Stewart R T *Solar Phys.* **75** 245 (1982)
189. Kane S R et al. *Astrophys. J.* **390** 687 (1992)
190. Vestrand W T, Forrest D J *Astrophys. J. Lett.* **409** L69 (1993)
191. Krucker S et al. *Astron. Astrophys. Rev.* **16** 155 (2008)
192. Masuda S et al. *Nature* **371** 495 (1994)
193. Krucker S, Lin R P *Astrophys. J.* **673** 1181 (2008)
194. Effenberger F et al. *Astrophys. J.* **835** 124 (2017)
195. Veronig A M, Brown J C *Astrophys. J.* **603** L117 (2004)
196. Xu Y, Emslie A G, Hurford G J *Astrophys. J.* **673** 576 (2008)
197. Fleishman G D et al. *Astrophys. J.* **816** 62 (2016)
198. Guo J et al. *Astron. Astrophys.* **543** A53 (2012)
199. Guo J, Emslie A G, Piana M *Astrophys. J.* **766** 28 (2013)
200. Fleishman G D et al. *Astrophys. J.* **857** 85 (2018)
201. Krucker S et al. *Astrophys. J.* **678** L63 (2008)
202. Hudson H S et al. *Astrophys. J.* **561** L211 (2001)
203. Krucker S, White S M, Lin R P *Astrophys. J.* **669** L49 (2007)
204. Cliver E W, Kahler S W, Vestrand W T, in *23rd Intern. Cosmic Ray Conf., ICRC23, 19 – 30 July, 1993, Alberta, Canada* Vol. 3 (Eds D A Leahy, R B Hicks, D Venkatesan) (Singapore: World Scientific, 1993) p. 91
205. Frost K J, Dennis B R *Astrophys. J.* **165** 655 (1971)
206. de Jager C, in *Solar Flares and Space Research, Proc. of a Symp., Tokyo, Japan, May 9 – 11, 1968* (Eds C de Jager, Z Svestka) (Amsterdam: North-Holland Publ. Co., 1969) p. 1
207. Hudson H S *Astrophys. J.* **224** 235 (1978)
208. Lastufka E et al. *Astrophys. J.* **886** 9 (2019)
209. Plotnikov I, Rouillard A P, Share G H *Astron. Astrophys.* **608** A43 (2017)
210. Jin M et al. *Astrophys. J.* **867** 122 (2018)
211. Vybornov V I et al. *Astron. Rep.* **56** 805 (2012); *Astron. Zh.* **89** 888 (2012)
212. Boynton W V et al. *Space Sci. Rev.* **110** 37 (2004)
213. Livshits M A et al. *Astron. Rep.* **61** 791 (2017); *Astron. Zh.* **94** 778 (2017)
214. Krucker S et al. *Res. Astron. Astrophys.* **19** 167 (2019)
215. Kuznetsov V D et al. *Geomag. Aeron.* **56** 781 (2016)